International Journal of Applied Earth Observations and Geoinformation 112 (2022) 102924

Contents lists available at ScienceDirect

International Journal of Applied Earth Observation and Geoinformation

journal homepage: www.elsevier.com/locate/jag

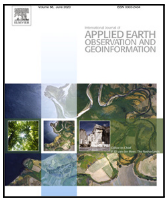

An adversarial learning approach to forecasted wind field correction with an application to oil spill drift prediction

Yongqing Li [a], Weimin Huang [b], Xinrong Lyu [c], Shanwei Liu [c], Zhe Zhao [c], Peng Ren [c,*]

[a] *College of Control Science and Engineering, China University of Petroleum (East China), Qingdao 266580, China*
[b] *Faculty of Engineering and Applied Science, Memorial University of Newfoundland, St. John's, NL A1B 3X5, Canada*
[c] *College of Oceanography and Space Informatics, China University of Petroleum (East China), Qingdao 266580, China*

ARTICLE INFO

Keywords:
Adversarial learning
ConvLSTM
Forecasted wind field correction
Oil spill drift prediction

ABSTRACT

Reanalysis wind fields are obtained by correcting the numerically forecasted wind fields based on observation data (i.e., either remote sensing or in-situ observations, or both). Although they are more accurate than forecasted wind fields, reanalysis wind fields tend to have time latencies because they can only be released after the observations are obtained. In order to produce accurate estimates of wind fields in a more timely manner, we develop an adversarial learning approach to correcting forecasted wind fields to be close to reanalysis wind fields. The adversarial learning approach is conducted by an adversarial ConvLSTM network (ACLN) framework that consists of a corrector and a discriminator. The corrector aims at comprehensively capturing both spatial and temporal characteristics of a sequence of forecasted wind fields and producing a corrected forecast wind field for the final field in the sequence. The discriminator tries to distinguish corrected forecast wind field from its corresponding reanalysis wind field. The training of ACLN is alternate between the corrector and the discriminator in an adversarial fashion. The adversarial training mechanism enhances the corrector's representational power. Additionally, the corrector exploits a residual learning architecture that effectively learns the differences between forecasted wind fields and the corresponding reanalysis wind fields. In this scenario, the well trained corrector requires neither reanalysis wind fields nor observations such that it can correct forecasted wind fields in a timely manner. Furthermore, corrected forecast wind fields are employed for oil spill drift prediction. Extensive experiments validate the effectiveness of the proposed ACLN framework in forecasted wind field correction along with oil spill drift prediction. Compared with ECMWF numerical forecasts, the ACLN achieves an average reduction of 6.2%, 6.9%, and 10.6% in RMSE, MAE, and MAPE, respectively. Compared with a basic drift prediction method, the ACLN based prediction method reduces the error by about 5000 m in the Sanchi oil spill accident. The source codes are available at https://github.com/liyongqingupc/ACLN-WindFieldCorrection, providing a baseline for correcting forecasted wind fields.

1. Introduction

Wind fields are comprehensive displays of wind information in a wide range. Wind field forecasts provide a promising approach to foreseeing future wind fields in advance and play an important role in operational tasks such as navigation safety and marine hazard prediction (Qi and Du, 2018). Existing methods for wind field forecast generally include numerical and machine learning based algorithms. In subsequent parts, the motivations, literature review, and limitations of these methods are presented. Then a brief description of the proposed approach is given along with an application of the approach. Finally, the major contributions of this paper are summarized.

1.1. Numerical wind field forecasts: Typical solutions

1.1.1. Motivations

Forecasted wind fields are produced by numerical equations that are based on physical laws and wind field variations (Zhuo et al., 2022). Analysis wind fields are obtained by assimilating forecasted wind fields with observations. To make forecasted wind fields consistent with future observations, the analysis wind fields are used to initialize subsequent numerical forecasts. However, the analysis wind fields may be limited by inadequate and poor-quality observations. On

---

* Corresponding author.
E-mail addresses: lyq_upc@163.com (Y. Li), weimin@mun.ca (W. Huang), lvxr@upc.edu.cn (X. Lyu), shanweiliu@163.com (S. Liu), zuckzhao@126.com (Z. Zhao), pengren@upc.edu.cn (P. Ren).

https://doi.org/10.1016/j.jag.2022.102924
Received 28 April 2022; Received in revised form 11 July 2022; Accepted 14 July 2022

Table 1
Timeliness descriptions of forecasted wind fields and reanalysis wind fields.

Institution	Product	Numerical forecast *horizon*	Reanalysis *latency*
NCEP	GFS	16 days	–
NCEP/NCAR	Reanalysis-1	–	24 days
NCEP/DOE	Reanalysis-2	–	24 days
ECMWF	ERA5	–	5 days

the other hand, reanalysis wind fields are dependent on a specific assimilation system. They require abundant high-quality remote sensing and in-situ observations (Zhang et al., 2017; Du et al., 2020) and have larger time latencies. Reanalysis wind fields are usually considered as accurate estimates of historical wind fields, even though they may still underestimate winds in coastal regions (Mayer et al., 2017).

1.1.2. Literature review

Numerical wind field forecasts have been studied for decades. National centers for environmental prediction (NCEP) developed a global forecast system (GFS) (Ma et al., 2015). European centre for medium-range weather forecasts (ECMWF) designed an integrated forecasting system (Roberts et al., 2018). NCEP and national center for atmospheric research (NCAR) developed a reanalysis-1 model (Kistler et al., 2001). NCEP and the department of energy (DOE) proposed a reanalysis-2 model (Kanamitsu et al., 2002). ECMWF successfully developed a series of reanalysis models including ERA-40 (Uppala et al., 2005), ERA-Interim (Dee et al., 2011), and ERA-5 (Nogueira, 2020). These forecast systems provide crucial forecast resources for research and practical applications.

1.1.3. Limitations

Forecasted wind fields and reanalysis wind fields at a global scale are mainly accessible from NCEP, NCAR, and ECMWF. Forecasted wind fields are available in advance but with limited forecast accuracy. reanalysis wind fields are considered as accurate wind field estimates but with many days of latency. The timeliness descriptions of the different data products are presented in Table 1. How to achieve both accuracy and timeliness of wind field forecasts is a challenging problem.

1.2. Machine learning based wind field forecasts: Recent progresses

1.2.1. Motivations

Machine learning based wind field forecasts (MLWFFs) are not limited by intricate numerical forecast models. They extract dynamic characteristics of historical wind field sequences and produce forecasted wind fields via nonlinear models. Given sufficient wind field data that are collected, the nonlinear models can be trained to characterize wind field variations and predict future wind fields.

1.2.2. Literature review

Machine learning has made great progresses in sequential characteristic extraction. Initially, many MLWFFs in a single-station fashion (i.e., wind speed forecasts) were developed. Barbounis et al. (2006) used different local recurrent neural networks for wind speed forecasts. Li and Shi (2010) investigated three networks for 1-h-ahead forecasts. Bhaskar and Singh (2012) used an adaptive wavelet neural network for forecasts. Guo et al. (2012) proposed a novel feed-forward neural network (FNN) for multi-step forecasts. Noman et al. (2021) developed a transfer learning model for multi-term forecasts. Shivam et al. (2020) developed a residual dilated U-net for short-term forecasts. Artificial neural networks (ANNs) (Cadenas and Rivera, 2010; Castellani et al., 2014), deep neural networks (DNNs) (Dalto et al., 2015; Hu et al., 2016), and long short-term memory (LSTM) networks (Liu et al., 2018; Hewage et al., 2019, 2021; Mudele et al., 2021) have been widely accepted for wind speed forecasts. Ibrahim et al. (2020) demonstrated that the ConvLSTM based forecast model outperformed the ANN, CNN, LSTM, and SVM models. Zhu et al. (2018) proposed a predictive deep CNN approach for wind field forecasts. Trebing and Mehrkanoon (2020) developed a multidimensional CNN for wind field forecasts. These methods perform well on short-term wind field forecasts given sufficient training data.

1.2.3. Limitations

MLWFFs are only driven by training data that are provided. There is no relevant physical laws underlying the forecast mechanisms. How to relate MLWFFs with physical laws is a challenging problem to solve.

1.3. Adversarial learning based forecasted wind field correction: Our novel approach

1.3.1. Motivations

Forecasted wind fields have limited forecast accuracy, while reanalysis wind fields are more accurate but with time latencies. MLWFFs have potential forecast abilities but lack relations with physical laws. One challenge to bridge numerical forecasts and MLWFFs is how to correct forecasted wind fields based on machine learning. In the light of these observations, in this study an adversarial ConvLSTM network (ACLN) is developed to correct forecasted wind fields to be close to reanalysis wind fields.

1.3.2. Related studies

In recent years, wind field corrections in a single-station fashion (i.e., wind speed corrections) have been investigated. Lauret et al. (2014) presented an ANN based method to improve numerical forecasts. Zjavka (2015) applied a differential polynomial neural network (DPNN) to correct wind speeds according to real observations. Liu et al. (2016) developed three wind speed correction methods including multiple linear regression and two neural networks. Buhan et al. (2016) proposed an ANN/SVM based model for correcting wind-electric forecasts. Tang et al. (2022) developed a light gradient boosting machine method to correct wind speeds from ECWMF for 18 observation stations. Nevertheless, these methods are all based on single-station wind speed correction. How to correct forecasted wind fields in a spatial fashion is an extremely crucial task.

1.3.3. Advantages of the proposed novel approach

The proposed ACLN approach integrates advantages of both forecasted wind fields and reanalysis wind fields. This approach learns the differences between forecasted wind fields and the corresponding reanalysis wind fields based on historical records. Reanalysis wind fields are generated by incorporating remote sensing and in-situ observations into numerical forecasts. Training with both forecasted wind fields and reanalysis wind fields enables ACLN to learn the knowledge of both the forecasts and observations. In practical operations, such an approach does not require either reanalysis wind fields or observations but can produce timely corrected forecast wind fields for forecasted wind fields based on the learned knowledge. In addition, this approach comprehensively captures both the spatial and temporal characteristics of the data sequence. Therefore, this approach not only relates physical laws but also considers the spatial and temporal characteristics of the input.

1.4. Application of the proposed approach to oil spill drift prediction

1.4.1. Motivations

Most existing oil spill drift prediction methods are driven by forecasted wind fields obtained from operational numerical forecast systems. However, forecasted wind fields have limited forecast accuracy. It is necessary to improve oil spill drift predictions via more accurate forecasted wind fields.

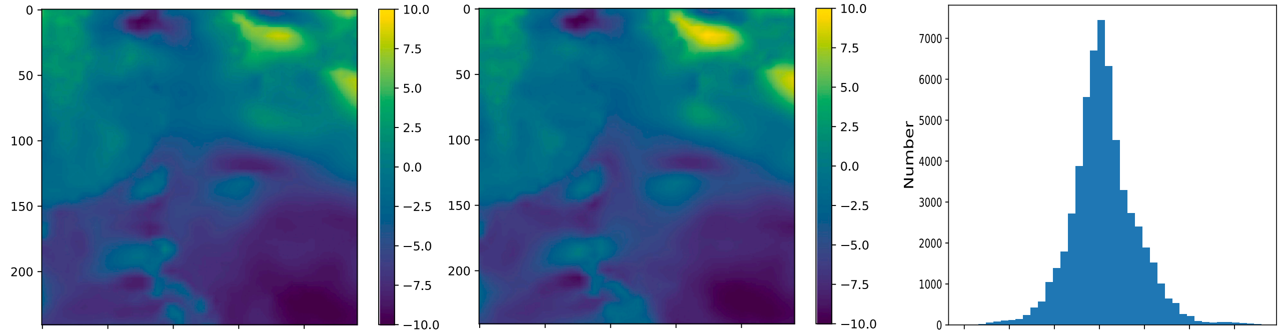

(a) Forecasted wind field in the u direction (b) Reanalysis wind field in the u direction (c) Histogram of wind field differences

Fig. 1. An example of (a) forecasted wind field (m/s), (b) reanalysis wind field (m/s), and (c) the histogram of wind field differences (m/s) on January 20th, 2018 at 12:00 UTC in the u direction.

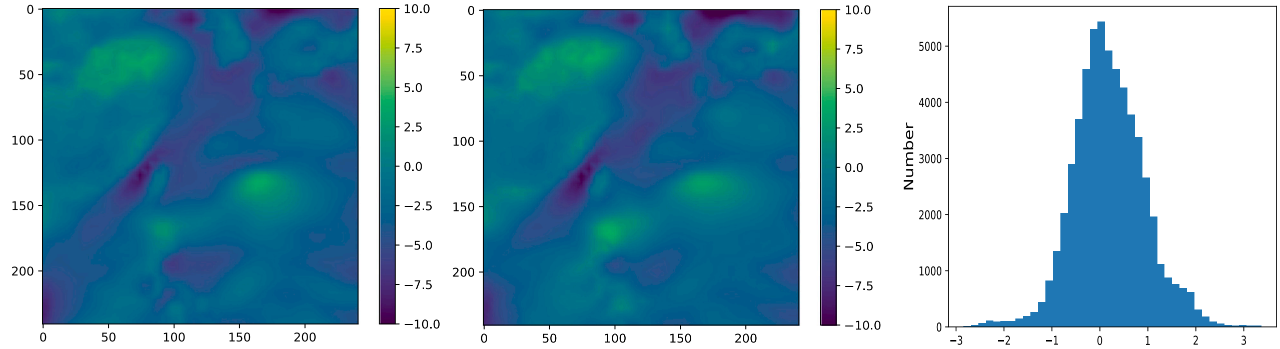

(a) Forecasted wind field in the v direction (b) Reanalysis wind field in the v direction (c) Histogram of wind field differences

Fig. 2. An example of (a) forecasted wind field (m/s), (b) reanalysis wind field (m/s), and (c) the histogram of wind field differences (m/s) on January 20th, 2018 at 12:00 UTC in the v direction.

Oil spill drift is generally determined by three components (Abascal et al., 2015): wind fields, current fields, and wave stokes drifts. Accurate wind fields would not only favor windage directly, but also enable high quality current fields obtained from ocean circulation models which take wind fields as input. Similarly, accurate wind fields also benefit wave simulation and are hence helpful for accurate Stokes drift prediction (Weisberg et al., 2017). Therefore, accurate wind fields would be in high favor of accurate oil spill drift prediction.

1.4.2. Related studies

Oil spill drift prediction is crucial for dynamically analyzing disasters and providing early warnings for related areas (Raimondi et al., 2017; De Moura et al., 2022). Lagrangian approaches are considered as effective numerical prediction models and represent oil spills using a large number of particles (Zodiatis et al., 2017). Liu et al. (2011a,b,c) were among the first to combine satellite images inferred oil spills with numerical ocean circulation models to predict the oil spill trajectories for rapid response to the Deepwater Horizon oil spills. Berry et al. (2012) developed an OILTRANS model and predicted accidental releases in the Celtic Sea. Cheng et al. (2014) tracked the trajectories of Gannet Alpha platform oil spills via an operational model. Jones et al. (2016) analyzed the transport characteristics of mineral and biogenic oil in the North Sea. Röhrs et al. (2018) investigated transport mechanisms based on an OpenOil model (Dagestad et al., 2018). Brekke et al. (2021) compared the oil drift simulations with remote sensing and in-situ observations. These studies reflect that oil spill drifts mainly depend on wind fields and current fields within the prediction range. Specifically, wind fields play a more dominant role in oil spill drifts for coastal ocean (Cheng et al., 2014).

1.4.3. Advantages of the proposed approach to oil spill drift prediction

The proposed wind field correction approach provides more accurate forecasted wind fields than numerically forecasted wind fields. In addition, this approach does not require assimilating wind field observations and provides corrected forecast wind fields with no time latencies. The application of such an approach to oil spill drift prediction is supposed to improve the prediction accuracy.

1.5. Novel contributions

(a) An adversarial learning approach is developed for forecasted wind field correction. The proposed approach takes advantage of both numerical and machine learning based methods. Training with both forecasted wind fields and reanalysis wind fields enables ACLN to learn from both forecasts and observations. On the other hand, it does not require observations in practical operations. Furthermore, it produces corrected forecast wind fields that are not only more accurate than forecasted wind fields but also more timely than reanalysis wind fields.

(b) This approach corrects forecasted wind fields in a spatial–temporal fashion. Different from existing single-station wind field correction methods, this approach is more comprehensive by capturing both the spatial and temporal characteristics of the forecasted wind field sequence.

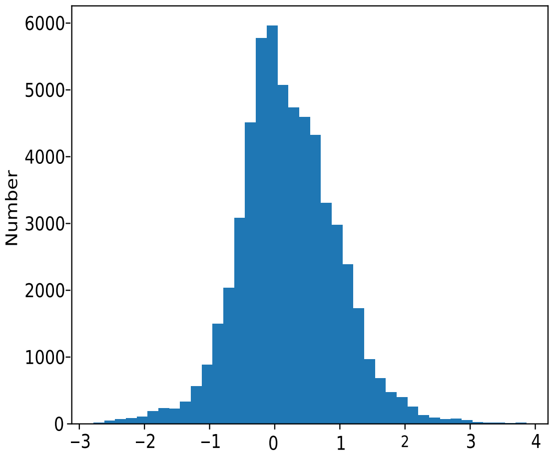

Fig. 3. The histogram of differences for the synthetic wind field (m/s) based on Figs. 1 and 2.

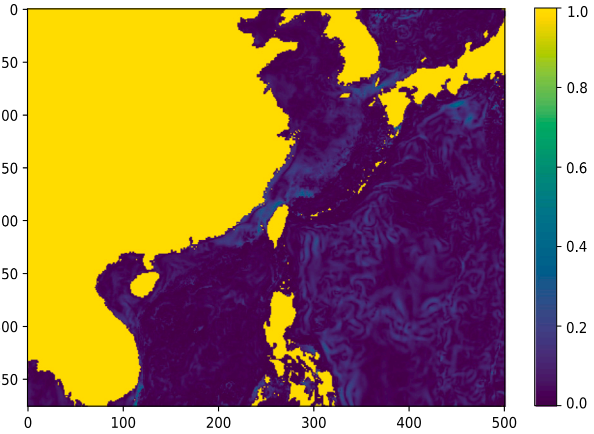

Fig. 4. A snapshot of the Global HYCOM simulated surface ocean currents (m/s) on January 18th, 2018 at 06:00 UTC.

(c) This approach achieves state-of-the-art performances for both the forecasted wind field correction and the application to oil spill drift prediction. The corresponding codes are released for public evaluations (see the Abstract).

2. Data for investigation

The wind field data set is obtained from an ERA-Interim archive of ECMWF.[1] The ERA-Interim provides coupled forecasted wind fields and reanalysis wind fields every day at 00:00, 06:00, 12:00, and 18:00 UTC separately. The wind field data set consists of data pairs, each of which includes a forecasted wind field and a reanalysis wind field at the same time. The ERA-Interim archive provides a benchmark for forecasted wind field correction. To investigate forecasted wind field correction and oil spill drift prediction in the East China Sea, the wind field data are downloaded within a square area with top left located at (40°N, 110°E) and bottom right located at (10°N, 140°E). The time span is from January 1st, 2018 to December 31th, 2018. Thus, 1,460 wind field data pairs are used to conduct experiments. The 1,336 data pairs from February to December are used to train the model and the 124 data pairs of January are for testing the correction performance.

Visual illustrations of wind components (u and v) on January 20th, 2018 at 12:00 UTC are presented in Figs. 1 and 2, respectively. Figs. 1(a) and 1(b) present forecasted wind field and reanalysis wind field in the u (eastward) direction, respectively. Fig. 1(c) shows the histogram of wind field differences between (a) and (b). Figs. 2(a) and 2(b) present forecasted wind field and reanalysis wind field in the v (northward) direction, respectively. Fig. 2(c) shows the histogram of wind field differences between (a) and (b). Let w_t^{u} and w_t^{v} denote the wind speed components in the u and v directions, respectively. The u and v directions are perpendicular to each other. The wind magnitude in the synthetic direction is formulated as $w_t = \sqrt{(w_t^{\mathrm{u}})^2 + (w_t^{\mathrm{v}})^2}$ and the wind direction is determined by $\arctan(w_t^{\mathrm{v}}/w_t^{\mathrm{u}})$. The two wind speed components contain both the magnitude and direction information of the wind speed. Fig. 3 shows the histogram of differences for the synthetic wind field based on Figs. 1 and 2. The differences between forecasted wind fields and reanalysis wind fields are mainly between $[-1, 1]$.

Forecasted current fields are downloaded from the Global HYCOM dataset GLBv0.08-expt_93.0.[2] The Global HYCOM output was used in the rapid response to the Deepwater Horizon oil spills in the Gulf of Mexico (Liu et al., 2011b,c). The spatial resolution is $0.08° \times 0.08°$ and the temporal resolution is 6 h. Fig. 4 shows a snapshot of the Global HYCOM simulated surface ocean currents on January 18th, 2018 at 06:00 UTC.

3. Adversarial learning approach to wind field correction

3.1. Adversarial approach

In this subsection, the mechanism of the proposed adversarial ConvLSTM network (ACLN) framework is described. Each wind field data sample contains u (eastward) component and v (northward) component, and each component is of $M \times N$ size. Let $\mathcal{W}_t \in \mathbb{R}^{2\times M\times N}$ denote a forecasted wind field at time t. The corresponding corrected forecast wind field denoted as $\widehat{\mathcal{W}}_t$ and reanalysis wind field denoted as $\widetilde{\mathcal{W}}_t$ have the same dimension as $\mathcal{W}_t$.

The main architecture of ACLN is illustrated in Fig. 5. The ACLN framework consists of a corrector and a discriminator. The corrector takes a forecasted wind field sequence $\{\mathcal{W}_{t-T}, \ldots, \mathcal{W}_{t-1}, \mathcal{W}_t\}$ as input and outputs $\widehat{\mathcal{W}}_t$ for $\mathcal{W}_t$. The discriminator takes $\widehat{\mathcal{W}}_t$ (or $\widetilde{\mathcal{W}}_t$) concatenating $\mathcal{W}_t$ as input and outputs a discriminant score that is high if the input is close to $\widetilde{\mathcal{W}}_t$. The corrector and discriminator are trained adversarially until the corrector has the capability of correcting forecasted wind fields effectively. The adversarial mechanism enhances the corrector's representational power and facilitates the corrector to output more accurate corrected forecast wind fields.

3.2. Corrector network

The corrector aims to extract the spatial and temporal characteristics of $\{\mathcal{W}_{t-T}, \ldots, \mathcal{W}_{t-1}, \mathcal{W}_t\}$ and output $\widehat{\mathcal{W}}_t$ for $\mathcal{W}_t$. The corrector consists of L ConvLSTM layers and one convolutional layer. Each ConvLSTM layer contains $T+1$ ConvLSTM cells whose number is governed by the length of the forecasted wind field sequence.

The internal structure of the lth ConvLSTM layer is illustrated in Fig. 5. $\{\mathcal{H}_{t-T}^{l}, \ldots, \mathcal{H}_{t-1}^{l}, \mathcal{H}_t^{l}\}$ and $\{\mathcal{C}_{t-T}^{l}, \ldots, \mathcal{C}_{t-1}^{l}, \mathcal{C}_t^{l}\}$ denote the short-term memories and the long-term memories produced by $T+1$ cells of the lth ConvLSTM layer, respectively. $\{\mathcal{W}_{t-T}, \ldots, \mathcal{W}_{t-1}, \mathcal{W}_t\}$ is considered as $\{\mathcal{H}_{t-T}^{0}, \ldots, \mathcal{H}_{t-1}^{0}, \mathcal{H}_t^{0}\}$. The input of the lth ConvLSTM layer is represented by $\{\mathcal{H}_{t-T}^{l-1}, \ldots, \mathcal{H}_{t-1}^{l-1}, \mathcal{H}_t^{l-1}\}$.

The architecture of the $(\tau+1)$th ConvLSTM cell in the lth ConvLSTM layer is illustrated in Fig. 6, where $0 \leqslant \tau \leqslant T$. The outputs of each cell are determined by its current input data and the output of a previous cell. $\mathcal{H}_{t-\tau}^{l-1}$ denotes the current input data of the $(\tau+1)$th cell. $\mathcal{H}_{t-\tau-1}^{l}$ and $\mathcal{C}_{t-\tau-1}^{l}$ denote the long-term memory and the short-term memory

---

[1] https://apps.ecmwf.int/datasets/data/interim-full-daily/levtype=sfc/

[2] http://tds.hycom.org/thredds/catalog.html

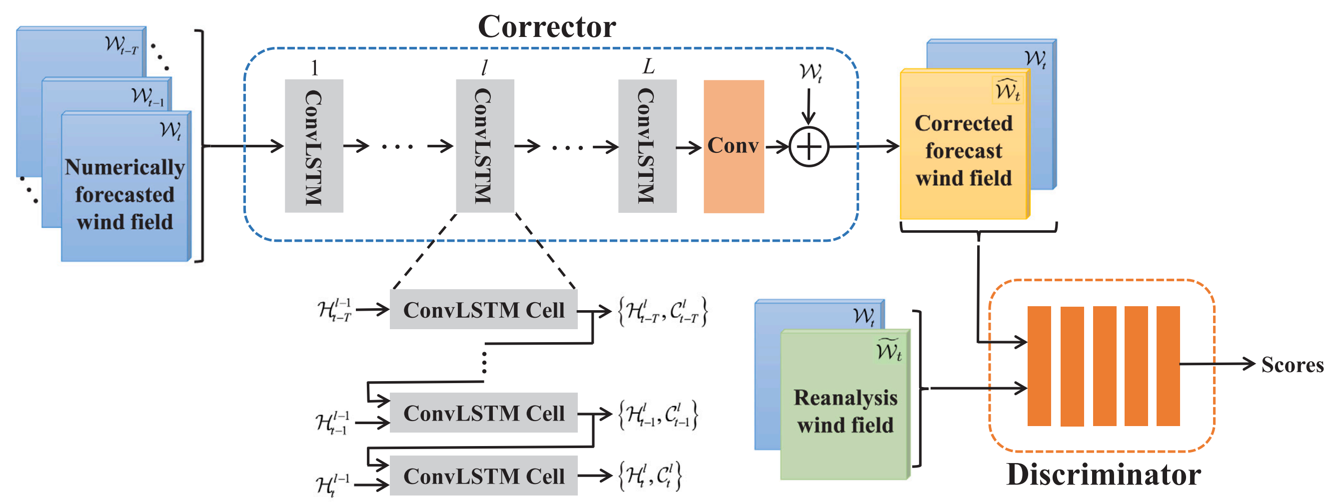

Fig. 5. The main architecture of the adversarial ConvLSTM network (ACLN) framework.

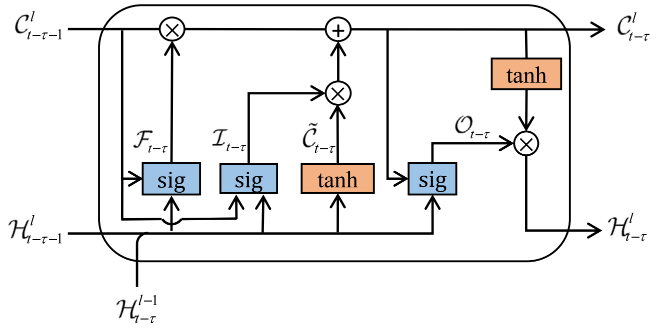

Fig. 6. The architecture of the $(\tau+1)$th ConvLSTM cell.

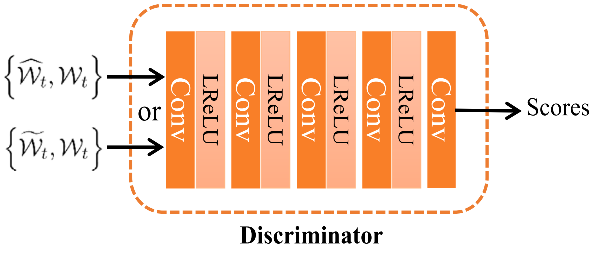

Fig. 7. The architecture of the discriminator network.

of $(\tau+2)$th cell, respectively. The $(\tau+1)$th cell takes $\mathcal{H}_{t-\tau}^{l-1}$, $\mathcal{C}_{t-\tau-1}^{l}$, and $\mathcal{H}_{t-\tau-1}^{l}$ together as input and outputs $\mathcal{C}_{t-\tau}^{l}$ and $\mathcal{H}_{t-\tau}^{l}$ that denote the updated long-term memory and short-term memory, respectively. In addition, the $(T+1)$th cell does not have the previous cell but only have $\mathcal{H}_{t-T}^{l-1}$ as input.

Each ConvLSTM cell consists of three gate controllers including a forget gate, an input gate, and an output gate. $\mathcal{X}_{\mathrm{f}1}$, $\mathcal{X}_{\mathrm{i}1}$, $\mathcal{X}_{\mathrm{c}1}$, and $\mathcal{X}_{\mathrm{o}1}$ denote the different convolution kernels for $\mathcal{H}_{t-\tau}^{l-1}$. $\mathcal{X}_{\mathrm{f}2}$, $\mathcal{X}_{\mathrm{i}2}$, $\mathcal{X}_{\mathrm{c}2}$, and $\mathcal{X}_{\mathrm{o}2}$ are the different convolution kernels for $\mathcal{H}_{t-\tau-1}^{l}$. $\mathcal{X}_{\mathrm{cf}}$ and $\mathcal{X}_{\mathrm{ci}}$ represent the product parameters for $\mathcal{C}_{t-\tau-1}^{l}$. $\mathcal{B}_{\mathrm{f}}$, $\mathcal{B}_{\mathrm{i}}$, and $\mathcal{B}_{\mathrm{c}}$ are corresponding bias variables.

$\mathcal{F}_{t-\tau}$ denotes the forget gate that controls the extent of forgetting. It is formulated as follows:

$$\mathcal{F}_{t-\tau} = \mathrm{sig}(\mathcal{X}_{\mathrm{f}1} * \mathcal{H}_{t-\tau}^{l-1} + \mathcal{X}_{\mathrm{f}2} * \mathcal{H}_{t-\tau-1}^{l} + \mathcal{X}_{\mathrm{cf}} \circ \mathcal{C}_{t-\tau-1}^{l} + \mathcal{B}_{\mathrm{f}}), \tag{1}$$

where $*$ denotes the convolution operator and $\circ$ indicates the Hadamard product, and $\mathrm{sig}(\cdot)$ is the sigmoid function.

$\mathcal{I}_{t-\tau}$ denotes the input gate that controls the extent to which new memory is written into long-term memory, and it can be written as:

$$\mathcal{I}_{t-\tau} = \mathrm{sig}(\mathcal{X}_{\mathrm{i}1} * \mathcal{H}_{t-\tau}^{l-1} + \mathcal{X}_{\mathrm{i}2} * \mathcal{H}_{t-\tau-1}^{l} + \mathcal{X}_{\mathrm{ci}} \circ \mathcal{C}_{t-\tau-1}^{l} + \mathcal{B}_{\mathrm{i}}). \tag{2}$$

$\widetilde{\mathcal{C}}_{t-\tau}$ represents the new memory that is derived from $\mathcal{H}_{t-\tau-1}^{l}$ and $\mathcal{H}_{t-\tau}^{l-1}$ as:

$$\widetilde{\mathcal{C}}_{t-\tau} = \tanh(\mathcal{X}_{\mathrm{c}1} * \mathcal{H}_{t-\tau}^{l-1} + \mathcal{X}_{\mathrm{c}2} * \mathcal{H}_{t-\tau-1}^{l} + \mathcal{B}_{\mathrm{c}}), \tag{3}$$

where $\tanh(\cdot)$ is the tanh activation function.

The updated long-term memory $\mathcal{C}_{t-\tau}^{l}$ is determined by the gated $\mathcal{C}_{t-\tau-1}^{l}$ and the gated $\widetilde{\mathcal{C}}_{t-\tau}$ as:

$$\mathcal{C}_{t-\tau}^{l} = \mathcal{F}_{t-\tau} \circ \mathcal{C}_{t-\tau-1}^{l} + \mathcal{I}_{t-\tau} \circ \widetilde{\mathcal{C}}_{t-\tau}. \tag{4}$$

$\mathcal{O}_{t-\tau}$ denotes the output gate that controls the extent to which the short-term memory is affected by the long-term memory, and it can be formulated as:

$$\mathcal{O}_{t-\tau} = \mathrm{sig}(\mathcal{X}_{\mathrm{o}1} * \mathcal{H}_{t-\tau}^{l-1} + \mathcal{X}_{\mathrm{o}2} * \mathcal{H}_{t-\tau-1}^{l} + \mathcal{X}_{\mathrm{co}} \circ \mathcal{C}_{t-\tau}^{l} + \mathcal{B}_{\mathrm{o}}), \tag{5}$$

where $\mathcal{X}_{\mathrm{co}}$ and $\mathcal{B}_{\mathrm{o}}$ are the product parameters for $\mathcal{C}_{t-\tau}^{l}$ and bias variable, respectively.

Then, the updated short-term memory $\mathcal{H}_{t-\tau}^{l}$ is:

$$\mathcal{H}_{t-\tau}^{l} = \mathcal{O}_{t-\tau} \circ \tanh(\mathcal{C}_{t-\tau}^{l}). \tag{6}$$

The Lth ConvLSTM layer outputs $\{\mathcal{H}_{t-T}^{L}, \dots, \mathcal{H}_{t-1}^{L}, \mathcal{H}_{t}^{L}\}$. The subsequent convolutional layer takes them as input and outputs $\mathcal{W}_t{}'$ as:

$$\mathcal{W}_t{}' = \mathrm{Conv}(\mathcal{H}_{t-T}^{L}, \dots, \mathcal{H}_{t-1}^{L}, \mathcal{H}_{t}^{L}), \tag{7}$$

where $\mathrm{Conv}(\cdot)$ represents the function of convolutional layer. As illustrated in Fig. 5, the corrector utilizes residual learning mechanism to learn the differences between the forecasted wind fields and the reanalysis wind fields. The corrected forecast wind field $\widehat{\mathcal{W}}_t$ is formulated as follows:

$$\widehat{\mathcal{W}}_t = \mathcal{W}_t + \mathcal{W}_t{}'. \tag{8}$$

The ConvLSTM layers play a key role in extracting spatial–temporal characteristics from the input sequence. Specifically, the convolutional parts of the ConvLSTM layers extract the spatial characteristics and the LSTM parts of the ConvLSTM layers extract the temporal characteristics. These extracted spatial–temporal characteristics are integrated by a convolutional layer to produce $\widehat{\mathcal{W}}_t$.

3.3. Discriminator network

As shown in Fig. 7, the discriminator consists of five convolutional layers in cascade with the first four followed by the LReLU activation

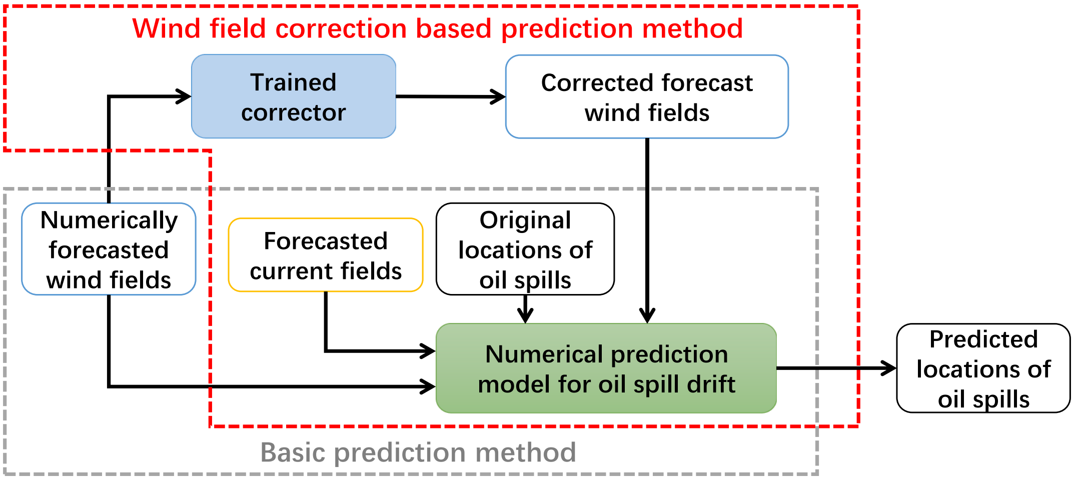

Fig. 8. Procedure of oil spill drift prediction methods.

layers. The discriminator takes $\left\{\widehat{\mathcal{W}}_t, \mathcal{W}_t\right\}$ or $\left\{\widetilde{\mathcal{W}}_t, \mathcal{W}_t\right\}$ as input and outputs a discriminant score S_D. $D(\cdot,\cdot)$ denotes the function representing the discriminator. S_D is determined as follows:

$$S_D = \begin{cases} D(\widehat{\mathcal{W}}_t, \mathcal{W}_t) & \text{for corrected data } \widehat{\mathcal{W}}_t \text{ as input,} \\ D(\widetilde{\mathcal{W}}_t, \mathcal{W}_t) & \text{for reanalysis data } \widetilde{\mathcal{W}}_t \text{ as input.} \end{cases} \tag{9}$$

S_D is the mean of the feature map produced by the final convolutional layer of the discriminator, and it is high if the input is close to $\widetilde{\mathcal{W}}_t$.

3.4. Training ACLN

The training loss L_{C_t} for the corrector is given as follows:

$$L_{C_t} = \lambda_1 \left\| \widetilde{\mathcal{W}}_t - \widehat{\mathcal{W}}_t \right\|_1 - D(\widehat{\mathcal{W}}_t, \mathcal{W}_t), \tag{10}$$

where λ_1 is a balance parameter, $\|\widetilde{\mathcal{W}}_t - \widehat{\mathcal{W}}_t\|_1$ is the ℓ_1 norm loss, and $-D(\widehat{\mathcal{W}}_t, \mathcal{W}_t)$ is the adversarial loss. Minimizing (10) means the corrector is trained to generate $\widehat{\mathcal{W}}_t$ as close to $\widetilde{\mathcal{W}}_t$ as possible. Finally, the corrector successfully fools the discriminator such that $\widehat{\mathcal{W}}_t$ and $\widetilde{\mathcal{W}}_t$ are assigned similar discriminant scores.

The training loss L_{D_t} for the discriminator is given as follows:

$$\begin{aligned} L_{D_t} = {} & D(\widehat{\mathcal{W}}_t, \mathcal{W}_t) - D(\widetilde{\mathcal{W}}_t, \mathcal{W}_t) \\ & + \lambda_2 \left(\left\| \nabla_{\overline{\mathcal{W}}_t} D(\overline{\mathcal{W}}_t, \mathcal{W}_t) \right\|_2 - 1 \right)^2, \end{aligned} \tag{11}$$

where λ_2 is a balance parameter, and $\overline{\mathcal{W}}_t$ is a random value sampled uniformly between $\widehat{\mathcal{W}}_t$ and $\widetilde{\mathcal{W}}_t$. $D(\widehat{\mathcal{W}}_t, \mathcal{W}_t) - D(\widetilde{\mathcal{W}}_t, \mathcal{W}_t)$ represents the adversarial loss that makes the discriminator try to classify $\widehat{\mathcal{W}}_t$ as false and $\widetilde{\mathcal{W}}_t$ as true. $\left(\left\|\nabla_{\overline{\mathcal{W}}_t} D(\overline{\mathcal{W}}_t, \mathcal{W}_t)\right\|_2 - 1\right)^2$ is the gradient penalty loss for stable gradients (Gulrajani et al., 2017). Minimizing (11) means the discriminator is trained to distinguish $\widehat{\mathcal{W}}_t$ from $\widetilde{\mathcal{W}}_t$.

The training procedure of ACLN is described in Algorithm 1. Specifically, the training of ACLN is performed alternately for the corrector and the discriminator. The corrector and the discriminator are adversarially trained such that their abilities of correction and discrimination are gradually improved, respectively. The adversarial training terminates when the discriminator cannot properly distinguish corrected forecast wind fields from reanalysis wind fields. In this scenario, the corrector and the discriminator achieve optimal representations together and cannot be improved by further adversarial training. Finally, the corrector is trained to be able to produce accurate corrected forecast wind fields.

3.5. Forecasted wind field correction

After the adversarial training described in Section 3.4, a trained corrector is ready for applications. In practical operations, the trained corrector takes a sequence of forecasted wind fields as input and outputs a corrected forecast wind field for the final field in the sequence. Though the corrector requires reanalysis wind fields for training, it does not require them in the practical operations. Therefore, the corrector can correct forecasted wind fields in a timely manner, i.e., it does not suffer from the time latencies that are associated with reanalysis wind fields.

4. Wind field correction based oil spill drift prediction

In this section, how to improve oil spill drift prediction based on the proposed wind field correction approach is described. To this end, a wind field correction based prediction method is developed. The essential idea of the developed method is to provide numerical prediction for oil spill drifts with more accurate wind field forecasts. A Lagrangian oil particle model is used as the basic prediction framework. It considers oil spills on a sea surface as a large concentration of particles. In this scenario, oil spill drifts are transformed into a superposition of particle movements. The particle movements are mainly driven by two crucial factors (Toz and Koseoglu, 2018; Nordam et al., 2019), i.e., wind fields and current fields. Therefore, the accuracy of oil spill drift prediction significantly depends on the forecast accuracies of these two fields.

A basic prediction method for oil spill drift is illustrated as the gray dashed box in Fig. 8. Forecasted wind fields, forecasted current fields, and original locations of oil spills are input into the numerical prediction model. The model outputs predicted locations of oil spills for specified time. The wind field correction based prediction method is illustrated as the red dashed box in Fig. 8. It utilizes the same numerical prediction model and forecasted current fields as the basic prediction method. The difference is that it takes corrected forecast wind fields as input instead of forecasted wind fields. Corrected forecast wind fields are obtained from a trained corrector as described in Section 3. Taking a single oil particle as an example, the oil particle model based prediction method is presented in the supplementary material.

The trained corrector has the capability of correcting numerically forecasted wind fields into those close to corresponding reanalysis wind fields. It provides more accurate forecasted wind fields than numerically forecasted wind fields. Therefore, it makes the wind field correction based prediction method output predicted coordinates of oil spill particles with higher accuracy than the basic prediction method.

Algorithm 1 Training procedure of the ACLN framework

```
Input: The training set consisting of forecasted wind fields and their corresponding reanalysis wind fields
Output: The trained parameter set of ACLN

for all training epochs do
    for all training samples do
        Input a forecasted wind field sequence $\{\mathcal{W}_{t-T}, \dots, \mathcal{W}_{t-1}, \mathcal{W}_t\}$ and a reanalysis wind field $\widetilde{\mathcal{W}}_t$;
        Compute $\widehat{\mathcal{W}}_t$ according to (8);
        Train discriminator: compute $L_{D_t}$ according to (11) and update parameters of the discriminator;
        Train corrector: compute $L_{C_t}$ according to (10) and update parameters of the corrector.
    end for
end for
```

Table 2

The parameter configuration for the ACLN framework.

Net	Layer	Filter	Kernel	Padding
Corrector	ConvLSTM	16	5 × 5	Same
	ConvLSTM	32	3 × 3	Same
	ConvLSTM	16	3 × 3	Same
	Conv	2	3 × 3	Same
Discriminator	Conv + LReLU	32	5 × 5	Same
	Conv + LReLU	64	3 × 3	Same
	Conv + LReLU	64	3 × 3	Same
	Conv + LReLU	32	3 × 3	Same
	Conv	1	3 × 3	Same

5. Experimental results and discussions

In this section, extensive experiments on the wind field data set obtained from ECMWF are conducted to evaluate the effectiveness of the proposed ACLN framework for forecasted wind field correction.

5.1. Experimental settings and evaluation metrics

To guarantee the precision of the forecasted wind field correction and oil spill drift prediction, we select the minimum spatial resolution $0.125^\circ \times 0.125^\circ$ and the minimum temporal resolution 6 h from multiple options. Each wind field data (i.e., forecasted or reanalysis wind field) with a size of 2 × 241 × 241 has two components (u and v). ACLN is implemented with Tensorflow 1.15.0 framework. A platform with 2 Intel Xeon Gold 5218R CPUs and 2 NVIDIA Geforce 2080Ti GPUs are used to deploy the experimental environment.

ACLN is composed of two parts, i.e., a corrector and a discriminator. To validate the effectiveness of ACLN, the correction performance of the corrector and the advantages of the discriminator are evaluated separately. The performance of ACLN is then compared with those of full convolutional network (FCN), ConvLSTM (Xingjian et al., 2015), and hierarchical generative adversarial network (HGAN) (Li et al., 2020). FCN is constructed with six full convolutional layers in cascade, where the kernel numbers of each layer are 64, 128, 256, 128, 64, 2 separately. The ConvLSTM network is implemented based on an open-source code.[3] HGAN is referred to an open-source code.[4]

The parameters for training ACLN in the experiments are set as follows. The number of ConvLSTM layers is set to 3. The length of the input sequence is 3. Batch normalization in the corrector with a batch size of 4 is used. The learning rate is set as 0.0005. The corrector is trained with a RMSProp optimizer, and the discriminator is trained with an Adam optimizer. The balance parameter λ_1 is set to 10, and the balance parameter λ_2 is 10. The parameter configuration for the ACLN framework is presented in Table 2.

Table 3

The average correction results for forecasted wind fields in u, v, and synthetic directions between January 18th, 2018 at 00:00 UTC and January 20th, 2018 at 18:00 UTC.

Direction	Method	RMSE	MAE	MAPE
u	NFM	0.8275	0.6081	99.9786
	FCN	0.7908	0.5848	90.2206
	ConvLSTM	0.7909	0.5882	91.5570
	HGAN	0.7865	0.5842	90.5423
	ACLN	**0.7781**	**0.5712**	**90.1009**
v	NFM	0.8807	0.6535	116.2239
	FCN	0.8395	0.6257	110.8776
	ConvLSTM	0.8441	0.6283	110.1663
	HGAN	0.8387	0.6246	108.8416
	ACLN	**0.8331**	**0.6172**	**106.6732**
Synthetic	NFM	0.8028	0.5819	16.0176
	FCN	0.7484	0.5471	14.8047
	ConvLSTM	0.7480	0.5498	15.0403
	HGAN	0.7397	0.5520	14.6434
	ACLN	**0.7339**	**0.5423**	**14.4043**

To evaluate the wind field correction performance, some quantitative evaluation criteria such as root mean squared error (RMSE), mean absolute error (MAE), and mean absolute percentage error (MAPE) are utilized. The magnitudes and directions of the wind fields are determined by its two components. It is necessary to evaluate the correction performance of each wind field component separately.

5.2. Comparisons with different deep learning methods

In this subsection, the effectiveness of ACLN is validated by comparing it with three different deep learning networks (FCN, ConvLSTM, and HGAN) and the numerical forecast model (NFM) (Dee et al., 2011). NFM provides a baseline for comparing the correction performances of four deep learning networks. FCN, ConvLSTM, and HGAN are separately trained and tested using the same data set as ACLN.

As shown in Fig. 9, the correction performances of four deep learning networks are compared in terms of RMSE, MAE, and MAPE for the period between January 18th, 2018 at 00:00 UTC and January 20th, 2018 at 18:00 UTC. The red lines in Fig. 9 represent the evaluation results of NFM and they are error baselines computed from forecasted wind fields and reanalysis wind fields at the same moments. A low curve reflects good correction performance. Three metrics of four deep learning networks are all below the red lines, i.e., better from those of NFM. It is also quantitatively demonstrated that four networks have achieved different correction degrees for forecasted wind fields. The correction performance of ACLN outperforms the other three networks. It is validated that ACLN captures more information from forecasted wind field sequences to output more accurate corrected forecast wind fields than the other three networks.

Table 3 illustrates the average correction results for forecasted wind fields in u, v, and synthetic directions between January 18th, 2018 at 00:00 UTC and January 20th, 2018 at 18:00 UTC. These correction

---

[3] https://github.com/giserh/ConvLSTM-2

[4] https://github.com/lihuiupc/HGAN-TyphoonCloudVisualPrediction

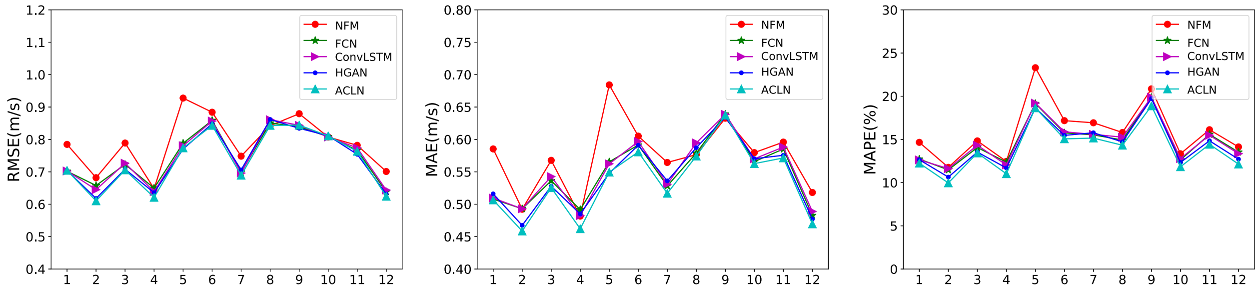

(a) RMSE (b) MAE (c) MAPE

Fig. 9. The correction performance comparison based on (a) RMSE, (b) MAE, and (c) MAPE of four methods between January 18th, 2018 at 00:00 UTC and January 20th, 2018 at 18:00 UTC.

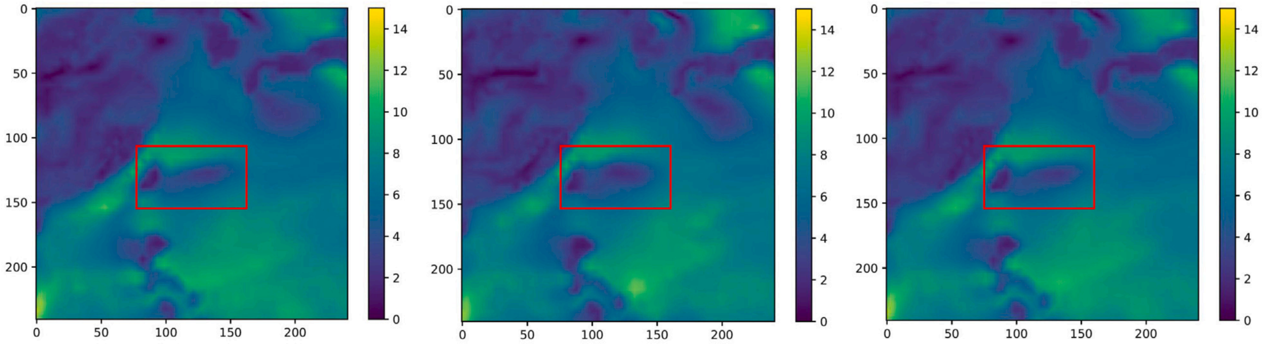

(a) Forecasted wind field (b) Reanalysis wind field (c) Corrected Forecast wind field

Fig. 10. The visual illustrations of (a) forecasted wind field (m/s), (b) reanalysis wind field (m/s), and (c) corrected forecast wind field (m/s) from ACLN on January 18th, 2018 at 12:00 UTC in the synthetic direction.

Table 4
The average correction results for the test set in the synthetic direction.

Method	Description	RMSE		MAE		MAPE	
		Non-Res	Res	Non-Res	Res	Non-Res	Res
NFM	Obtained from ECMWF	0.9620	–	0.7074	–	15.5899	–
FCN	Single network	0.9224	0.9167	0.6795	0.6725	14.6994	14.6128
ConvLSTM	Single network	0.9302	0.9188	0.6812	0.6698	14.7224	14.6458
HGAN	Adversarial networks	**0.9205**	0.9089	0.6787	0.6656	14.6217	14.4327
ACLN	Adversarial networks	0.9210	**0.9022**	**0.6779**	**0.6587**	**14.3365**	**13.9364**

results comprehensively evaluate both the magnitudes and directions of the wind fields in terms of u and v components. It is quantitatively validated that the correction errors of ACLN are all less than those of the other three methods.

Table 4 lists the average correction results for the test set in the synthetic direction. Compared with NFM, ACLN has achieved an average of 6.2% reduction in RMSE, an average of 6.9% reduction in MAE, and an average of 10.6% reduction in MAPE on the test set. To evaluate the effectiveness of the residual learning architecture in ACLN, the same residual mechanism is employed to FCN, ConvLSTM, and HGAN separately. Furthermore, the residual mechanism of ACLN is deleted to test its correction performance. As shown in Table 4, the correction performances of four methods are compared in terms of whether based on the residual mechanism or not. It is obviously shown that all networks with the residual mechanism have better correction performances than those without the residual mechanism. In addition, FCN and ConvLSTM are single networks, HGAN and ACLN are adversarial networks. As shown in Table 4, the correction performances of adversarial networks are better than those of single networks. It is demonstrated that discriminators have advantages in facilitating correctors to output more accurate correction results.

Therefore, with regard to three evaluation criteria, the overall correction performance of the proposed ACLN framework outperforms the other three methods. Wind field correction based oil spill drift prediction is generally conducted at a large time scale. Comparatively small improvements in wind fields can result in large drift accuracy improvements. The ACLN is a general method that is not only constrained to correct wind fields but also can be extended to other geophysical parameter correction if both the forecasted data and reanalysis data for the geophysical parameter are available for model training. Therefore, it is worth investigating the performance of using the ACLN to correct other geophysical parameters.

5.3. Simulated oil spill drift prediction

In this subsection, the effectiveness of wind field correction based prediction method on simulated oil spill drift prediction is tested. Section 5.2 has demonstrated that the proposed ACLN has a better wind field correction performance. As shown in Fig. 10, corrected forecast wind field (Fig. 10(c)), especially in the red box area, is visually more similar to reanalysis wind field (Fig. 10(b)) than forecasted wind field (Fig. 10(a)). The same situation is shown in Figs. 11 and 12. These corrected forecast wind fields from ACLN are utilized for oil spill drift predictions. As reanalysis current fields are difficult to obtain, current field correction still remains a big challenging issue. The forecasted current fields downloaded from the Global HYCOM dataset are utilized for

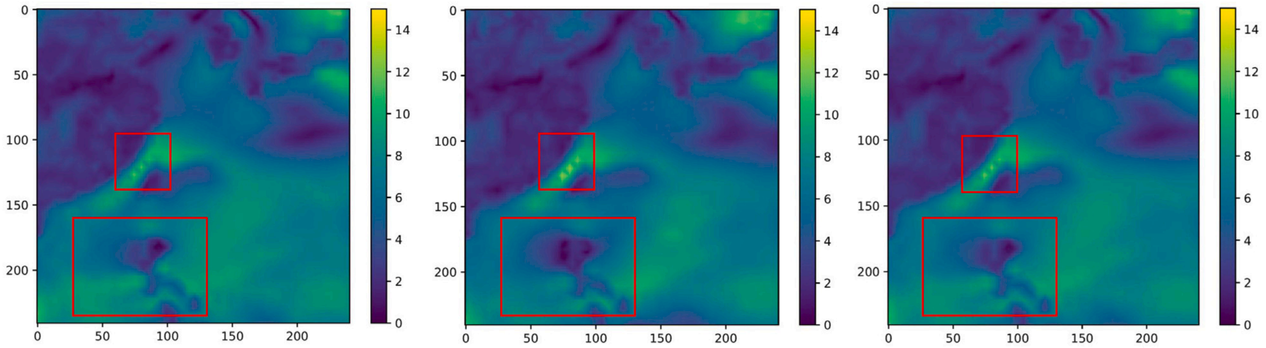

(a) Forecasted wind field (b) Reanalysis wind field (c) Corrected forecast wind field

Fig. 11. The visual illustrations of (a) forecasted wind field (m/s), (b) reanalysis wind field (m/s), and (c) corrected forecast wind field (m/s) from ACLN on January 18th, 2018 at 18:00 UTC in the synthetic direction.

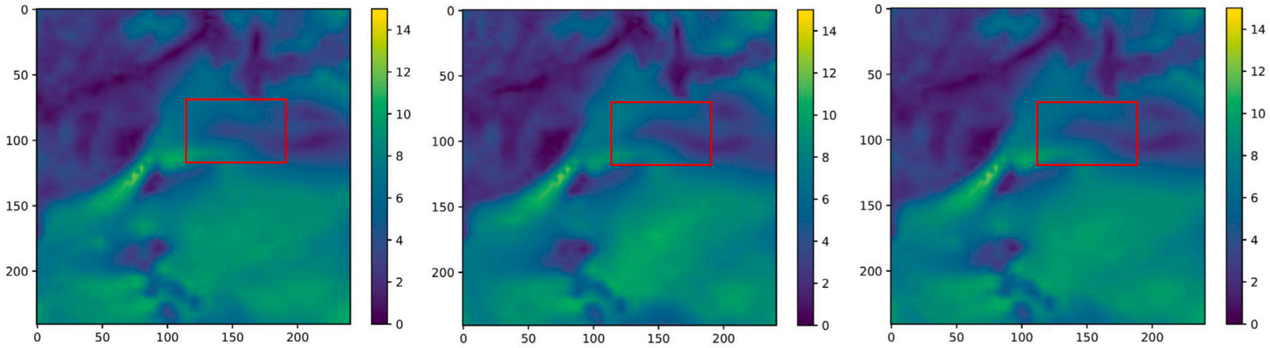

(a) Forecasted wind field (b) Reanalysis wind field (c) Corrected forecast wind field

Fig. 12. The visual illustrations of (a) forecasted wind field (m/s), (b) reanalysis wind field (m/s), and (c) corrected forecast wind field (m/s) from ACLN on January 19th, 2018 at 00:00 UTC in the synthetic direction.

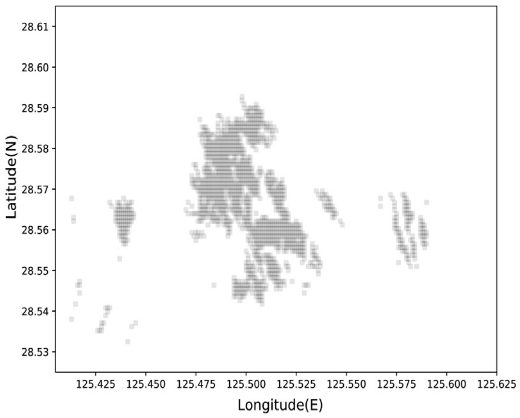

Fig. 13. The original locations of oil spills on January 18th, 2018 at 06:00 UTC.

oil spill drift predictions. To intuitively illustrate oil spills, we randomly initialize 1,474 oil spill particles used for simulated experiments. As shown in Fig. 13, the black dots represent the original locations of the oil spill particles on January 18th, 2018 at 06:00 UTC.

As shown in Fig. 14, the blue dots and the yellow dots represent the oil spill drift prediction results based on forecasted wind fields and reanalysis wind fields, respectively. As the prediction goes further in time, the location distances between the blue dots and the yellow dots gradually increase. As shown in Fig. 15, the blue and yellow dots represent the oil spill drift prediction results based on corrected forecast wind fields and reanalysis wind fields, respectively. The prediction results based on reanalysis wind fields are regarded as true drift results. By comparing Figs. 14 and 15, it can be seen that the prediction results based on corrected forecast wind fields are closer to the true drift results than those based on forecasted wind fields.

To quantitatively evaluate the prediction results of simulated oil spill drifts, the average longitude errors and latitude errors are calculated based on the prediction results in Figs. 14 and 15.

Table 5 shows the average prediction errors based on the basic prediction method and the wind field correction based prediction method. It is clear that the longitude errors of wind field correction based prediction method are slightly lower than those of the basic prediction method and the latitude errors of that are much lower than those of the basic prediction method. The simulated experiments of oil spill drift prediction validate that the wind field correction based prediction method is in favor of oil spill drift prediction.

5.4. Practical oil spill drift prediction

In order to further test the effectiveness of the wind field correction based prediction method, the data from the Sanchi oil spill accident that happened in the East China Sea on January 6th, 2018 (Qiao et al., 2019) are used. The oil tanker Sanchi caught fire after the collision and sank on January 14th, 2018. A large amount of condensate oil and fuel oil are leaked on the sea surface. Two remote sensing images containing Sanchi oil spills are downloaded for this study.

Fig. 16(a) illustrates the remote sensing image captured by Sentinel-2 satellite on January 18th, 2018 at 02:20 UTC. Fig. 16(b) shows the image patch containing Sanchi oil spills. Fig. 16(c) displays the labeled oil spill locations. Fig. 17(a) illustrates the remote sensing image captured by GF-1 satellite on January 20th, 2018 at 11:17 UTC.

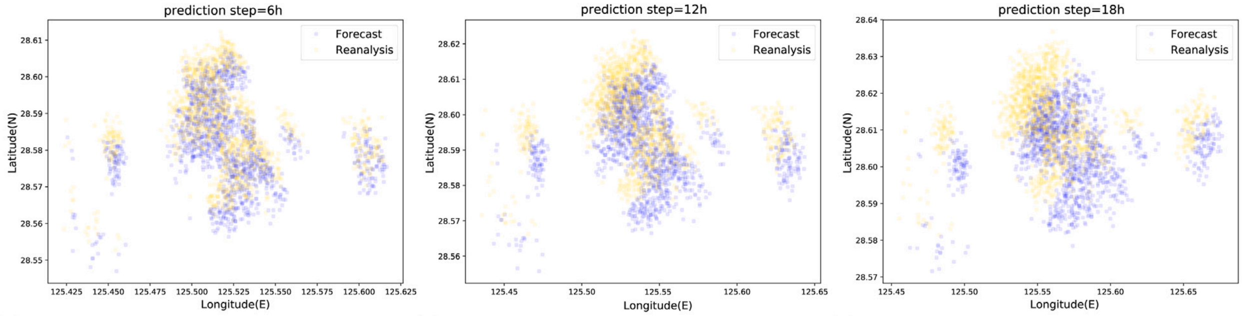

(a) Prediction results on January 18th, 2018 at 12:00 UTC. (b) Prediction results on January 18th, 2018 at 18:00 UTC. (c) Prediction results on January 19th, 2018 at 00:00 UTC.

Fig. 14. The prediction results of oil spill drift based on forecasted wind fields (blue dots) and reanalysis wind fields (yellow dots). (For interpretation of the references to color in this figure legend, the reader is referred to the web version of this article.)

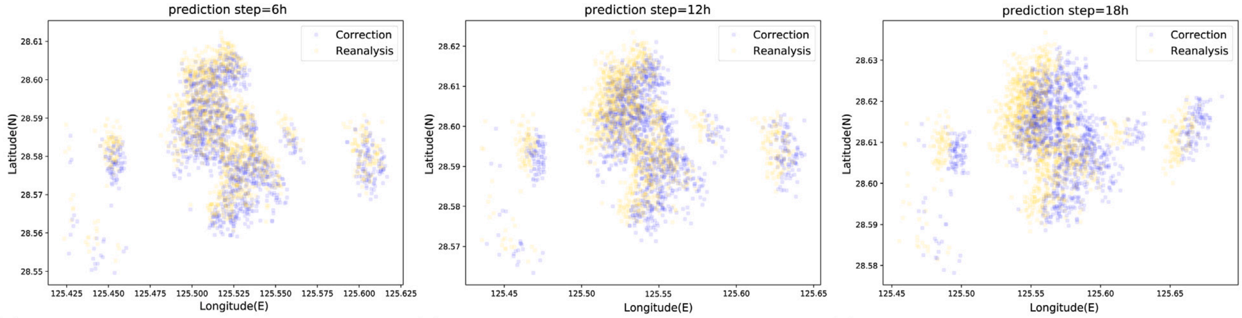

(a) Prediction results on January 18th, 2018 at 12:00 UTC. (b) Prediction results on January 18th, 2018 at 18:00 UTC. (c) Prediction results on January 19th, 2018 at 00:00 UTC.

Fig. 15. The prediction results of oil spill drift based on corrected forecast wind fields (blue dots) and reanalysis wind fields (yellow dots). (For interpretation of the references to color in this figure legend, the reader is referred to the web version of this article.)

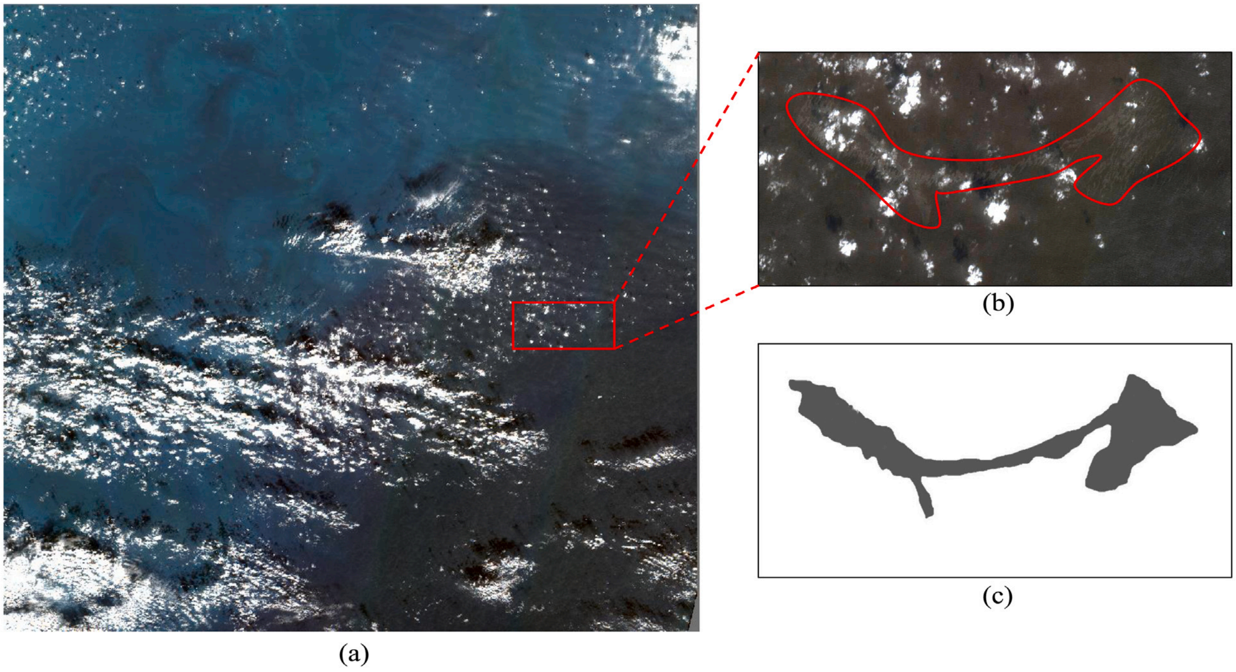

Fig. 16. (a) The Sanchi oil spill observation image captured by Sentinel-2 satellite on January 18th, 2018 at 02:20 UTC; (b) The image patch containing Sanchi oil spills (red); (c) The labeled oil spill locations in (b). (For interpretation of the references to color in this figure legend, the reader is referred to the web version of this article.)

Table 5
The average prediction errors based on the basic prediction method and the wind field correction based prediction method.

Prediction step	Basic prediction method		Wind field correction based prediction method	
	Longitude error (°)	Latitude error (°)	Longitude error (°)	Latitude error (°)
6 h	2.2402×10^{-3}	4.6487×10^{-3}	2.2178×10^{-3}	1.9491×10^{-3}
12 h	6.5633×10^{-3}	7.1203×10^{-3}	6.3966×10^{-3}	2.6901×10^{-3}
18 h	1.1926×10^{-2}	7.7975×10^{-3}	1.0195×10^{-2}	2.6894×10^{-3}

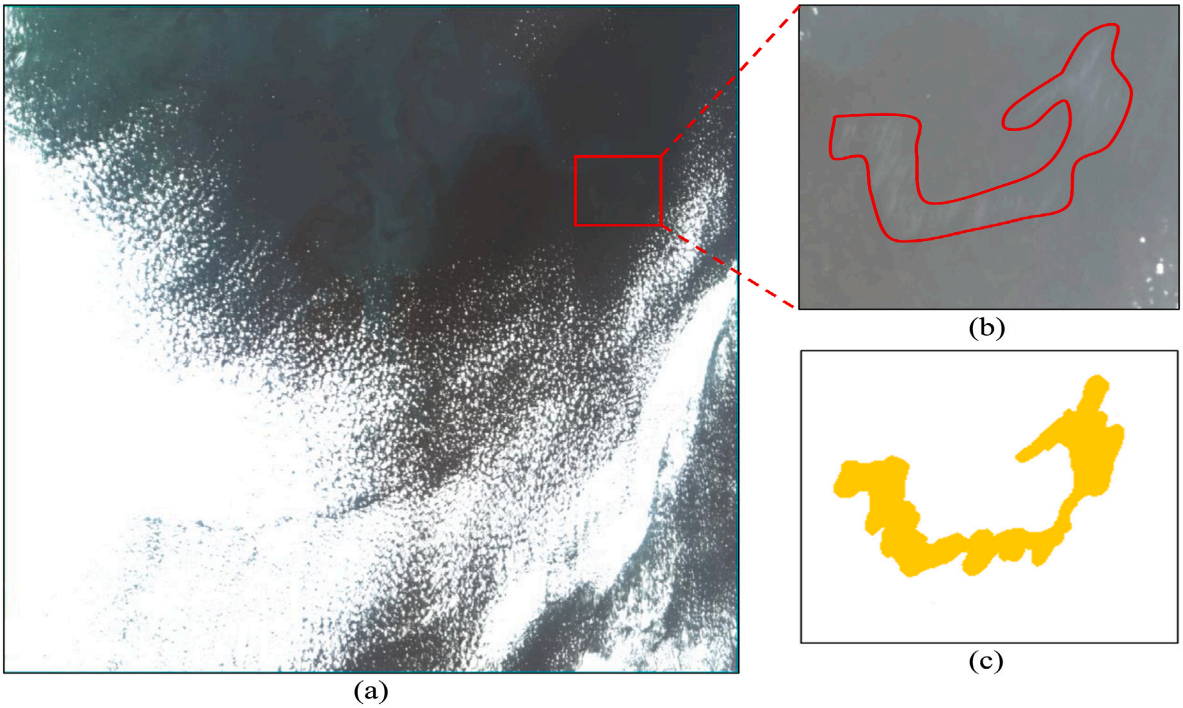

Fig. 17. (a) The Sanchi oil spill observation image captured by GF-1 satellite on January 20th, 2018 at 11:17 UTC; (b) The image patch containing Sanchi oil spills (red); (c) The labeled oil spill locations in (b). (For interpretation of the references to color in this figure legend, the reader is referred to the web version of this article.)

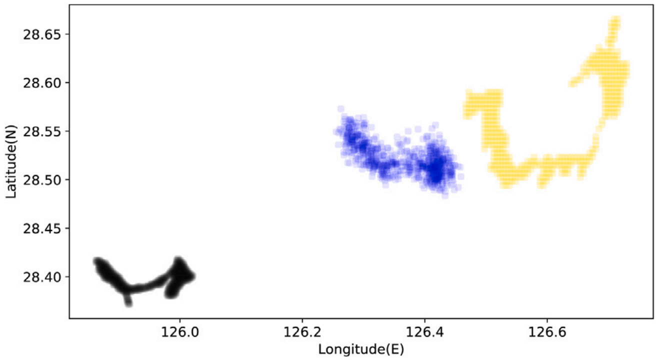

Fig. 18. The predicted oil spill drift results (blue dots) based on forecasted wind fields. The black dots indicate original oil spill locations and the yellow dots denote true oil spill drift results. (For interpretation of the references to color in this figure legend, the reader is referred to the web version of this article.)

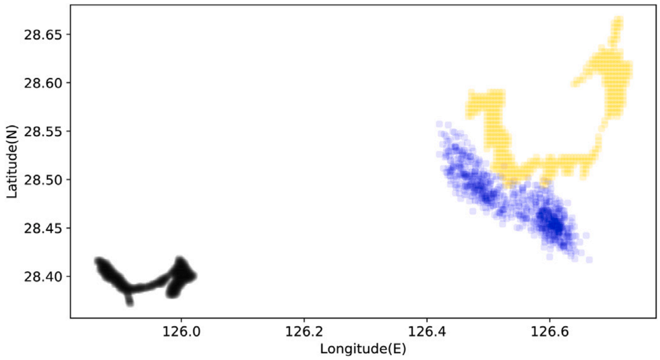

Fig. 19. The predicted oil spill drift results (blue dots) based on corrected forecast wind fields. The black dots indicate original oil spill locations and the yellow dots denote true oil spill drift results. (For interpretation of the references to color in this figure legend, the reader is referred to the web version of this article.)

Fig. 17(b) shows the image patch containing Sanchi oil spills. Fig. 17(c) displays the labeled oil spill locations.

As shown in Figs. 18 and 19, the blue dots represent predicted oil spill drift results. The black dots indicate original oil spill locations and the yellow dots denote true oil spill drift results. By comparing Figs. 18 and 19, we observe that the predicted results based on corrected forecast wind fields are more close to true oil spill drift results than those based on forecasted wind fields. Compared with the basic prediction method, the wind field correction based prediction method reduces the error by about 5000 m in the Sanchi oil spill accident. It is demonstrated that the proposed prediction method achieves more accurate oil spill drift prediction.

Although the predicted results in Fig. 19 are better than those in Fig. 18, they still deviate from the true drift results. One possible reason is that the minimum temporal resolution available for wind fields is 6 h, and the oil spill drift prediction model is driven at a coarse time scale. This observation suggests that increasing the temporal resolution of wind field forecasts can reasonably increase the accuracy of oil spill drift prediction.

6. Conclusions

In this paper, an adversarial learning approach is developed for correcting forecasted wind fields to be close to reanalysis wind fields. The adversarial learning approach is conducted by an ACLN framework. In contrast to reanalysis products, the proposed approach does not require observations and can provide corrected forecast wind fields in a timely manner. Compared with NFM, ACLN has achieved an average reduction of 6.2%, 6.9%, and 10.6% in RMSE, MAE, and MAPE, respectively. Furthermore, an application of corrected forecast wind fields for oil spill drift prediction is introduced. Compared with the basic drift prediction method, the proposed prediction method can reduce the error by about 5000 m in the Sanchi oil spill accident. These experiments have validated the effectiveness of ACLN.

A more comprehensive oil spill drift prediction model that can describe oil spills in details under complex marine environment may be developed. It can be accomplished in terms of several aspects. Firstly, a regional or coastal ocean circulation model instead of the Global HYCOM can be used for the ocean currents. Secondly, a Stokes drift component, which is important in transporting oil to beaches (Weisberg et al., 2017), can be considered in the oil spill drift model. Thirdly, more advanced skill scores can be used to quantify the performance of oil spill trajectory modeling (Liu and Weisberg, 2011; Dearden et al., 2021).

CRediT authorship contribution statement

Yongqing Li: Conceptualization, Methodology, Software, Visualization, Writing – original draft, Writing – review & editing. **Weimin Huang:** Conceptualization, Methodology, Writing – review & editing. **Xinrong Lyu:** Methodology, Writing – review & editing. **Shanwei Liu:** Conceptualization, Methodology, Writing – review & editing. **Zhe Zhao:** Software, Visualization, Methodology, Writing – review & editing. **Peng Ren:** Conceptualization, Funding acquisition, Validation, Formal analysis, Resources, Supervision, Software, Visualization, Writing – review & editing.

Declaration of competing interest

The authors declare that they have no known competing financial interests or personal relationships that could have appeared to influence the work reported in this paper.

Acknowledgments

This work was supported in part by the National Natural Science Foundation of China [Grant Number 61971444]; in part by the Shandong Provincial Natural Science Foundation, China [Grant Number ZR2019MF019]; and in part by the National Key Research and Development Program of China [Grant Number 2017YFC1405600].

Appendix A. Supplementary data

Supplementary material related to this article can be found online at https://doi.org/10.1016/j.jag.2022.102924.

References

Abascal, A.J., Castanedo, S., Minguez, R., Medina, R., Liu, Y., Weisberg, R.H., 2015. Stochastic Lagrangian trajectory modeling of surface drifters deployed during the deepwater horizon oil spill. In: Proceedings of the Thirty-Eighth AMOP Technical Seminar; Environment Canada: Ottawa, on, Canada. pp. 77–91.

Barbounis, T.G., Theocharis, J.B., Alexiadis, M.C., Dokopoulos, P.S., 2006. Long-term wind speed and power forecasting using local recurrent neural network models. IEEE Trans. Energy Convers. 21 (1), 273–284.

Berry, A., Dabrowski, T., Lyons, K., 2012. The oil spill model OILTRANS and its application to the Celtic Sea. Mar. Pollut. Bull. 64 (11), 2489–2501.

Bhaskar, K., Singh, S.N., 2012. AWNN-assisted wind power forecasting using feed-forward neural network. IEEE Trans. Sustain. Energy 3 (2), 306–315.

Brekke, C., Espeseth, M.M., Dagestad, K.-F., Röhrs, J., Hole, L.R., Reigber, A., 2021. Integrated analysis of multisensor datasets and oil drift simulations—A free-floating oil experiment in the open ocean. J. Geophys. Res. Oceans 126 (1), e2020JC016499.

Buhan, S., Özkazanç, Y., Çadırcı, I., 2016. Wind pattern recognition and reference wind mast data correlations with NWP for improved wind-electric power forecasts. IEEE Trans. Ind. Inf. 12 (3), 991–1004.

Cadenas, E., Rivera, W., 2010. Wind speed forecasting in three different regions of Mexico, using a hybrid ARIMA–ANN model. Renew. Energy 35 (12), 2732–2738.

Castellani, F., Burlando, M., Taghizadeh, S., Astolfi, D., Piccioni, E., 2014. Wind energy forecast in complex sites with a hybrid neural network and CFD based method. Energy Procedia 45, 188–197.

Cheng, Y., Liu, B., Li, X., Nunziata, F., Xu, Q., Ding, X., Migliaccio, M., Pichel, W.G., 2014. Monitoring of oil spill trajectories with COSMO-SkyMed X-band SAR images and model simulation. IEEE J. Sel. Top. Appl. Earth Obs. Remote Sens. 7 (7), 2895–2901.

Dagestad, K.-F., Röhrs, J., Breivik, Ø., Ådlandsvik, B., 2018. OpenDrift v1. 0: a generic framework for trajectory modelling. Geosci. Model Dev. 11 (4), 1405–1420.

Dalto, M., Matuško, J., Vašak, M., 2015. Deep neural networks for ultra-short-term wind forecasting. In: 2015 IEEE International Conference on Industrial Technology. ICIT, IEEE, pp. 1657–1663.

De Moura, N.V.A., de Carvalho, O.L.F., Gomes, R.A.T., Guimarães, R.F., de Carvalho Júnior, O.A., 2022. Deep-water oil-spill monitoring and recurrence analysis in the Brazilian territory using Sentinel-1 time series and deep learning. Int. J. Appl. Earth Obs. Geoinf. 107, 102695.

Dearden, C., Culmer, T., Brooke, R., 2021. Performance measures for validation of oil spill dispersion models based on satellite and coastal data. IEEE J. Ocean. Eng. 47 (1), 126–140.

Dee, D.P., Uppala, S.M., Simmons, A., Berrisford, P., Poli, P., Kobayashi, S., Andrae, U., Balmaseda, M., Balsamo, G., Bauer, d.P., et al., 2011. The ERA-Interim reanalysis: Configuration and performance of the data assimilation system. Q. J. R. Meteorol. Soc. 137 (656), 553–597.

Du, Y., Yang, X., Yang, J., Tan, S., Ma, W., Li, Z., Li, X., 2020. Effects of temperature on sea surface radar backscattering under neutral and nonneutral atmospheric conditions for wind retrieval applications: a numerical study. IEEE Trans. Geosci. Remote Sens. 59 (4), 2727–2743.

Gulrajani, I., Ahmed, F., Arjovsky, M., Dumoulin, V., Courville, A., 2017. Improved training of wasserstein gans. arXiv preprint arXiv:1704.00028.

Guo, Z., Zhao, W., Lu, H., Wang, J., 2012. Multi-step forecasting for wind speed using a modified EMD-based artificial neural network model. Renew. Energy 37 (1), 241–249.

Hewage, P., Behera, A., Trovati, M., Pereira, E., 2019. Long-short term memory for an effective short-term weather forecasting model using surface weather data. In: IFIP International Conference on Artificial Intelligence Applications and Innovations. Springer, pp. 382–390.

Hewage, P., Trovati, M., Pereira, E., Behera, A., 2021. Deep learning-based effective fine-grained weather forecasting model. Pattern Anal. Appl. 24 (1), 343–366.

Hu, Q., Zhang, R., Zhou, Y., 2016. Transfer learning for short-term wind speed prediction with deep neural networks. Renew. Energy 85, 83–95.

Ibrahim, M., Alsheikh, A., Al-Hindawi, Q., Al-Dahidi, S., ElMoaqet, H., 2020. Short-time wind speed forecast using artificial learning-based algorithms. Comput. Intell. Neurosci. 2020.

Jones, C.E., Dagestad, K.-F., Breivik, Ø., Holt, B., Röhrs, J., Christensen, K.H., Espeseth, M., Brekke, C., Skrunes, S., 2016. Measurement and modeling of oil slick transport. J. Geophys. Res. Oceans 121 (10), 7759–7775.

Kanamitsu, M., Ebisuzaki, W., Woollen, J., Yang, S.-K., Hnilo, J., Fiorino, M., Potter, G., 2002. Ncep–doe amip-ii reanalysis (r-2). Bull. Am. Meteorol. Soc. 83 (11), 1631–1644.

Kistler, R., Kalnay, E., Collins, W., Saha, S., White, G., Woollen, J., Chelliah, M., Ebisuzaki, W., Kanamitsu, M., Kousky, V., et al., 2001. The NCEP–NCAR 50-year reanalysis: monthly means CD-ROM and documentation. Bull. Am. Meteorol. Soc. 82 (2), 247–268.

Lauret, P., Diagne, H.M., David, M., 2014. A neural network post-processing approach to improving NWP solar radiation forecasts. Energy Procedia 57, 1044–1052.

Li, H., Gao, S., Liu, G., Guo, D., Grecos, C., Ren, P., 2020. Visual prediction of typhoon clouds with hierarchical generative adversarial networks. IEEE Geosci. Remote Sens. Lett. 17 (9), 1478–1482.

Li, G., Shi, J., 2010. On comparing three artificial neural networks for wind speed forecasting. Appl. Energy 87 (7), 2313–2320.

Liu, Y., Macfadyen, A., Ji, Z.G., Weisberg, R.H., 2011a. Monitoring and modeling the deepwater horizon oil spill: A record-breaking enterprise. Geophys. Monogr. Ser. 195, 271. http://dx.doi.org/10.1029/GM195, (Washington, D.C., USA: AGU/geopress).

Liu, H., Mi, X., Li, Y., 2018. Smart deep learning based wind speed prediction model using wavelet packet decomposition, convolutional neural network and convolutional long short term memory network. Energy Convers. Manage. 166, 120–131.

Liu, Y., Wang, Y., Li, L., Han, S., Infield, D., 2016. Numerical weather prediction wind correction methods and its impact on computational fluid dynamics based wind power forecasting. J. Renew. Sustain. Energy 8 (3), 033302.

Liu, Y., Weisberg, R.H., 2011. Evaluation of trajectory modeling in different dynamic regions using normalized cumulative Lagrangian separation. J. Geophys. Res. Oceans 116 (C9).

Liu, Y., Weisberg, R.H., Hu, C., Zheng, L., 2011b. Tracking the Deepwater Horizon oil spill: A modeling perspective. EOS Trans. Am. Geophys. Union 92 (6), 45–46. http://dx.doi.org/10.1029/2011EO060001.

Liu, Y., Weisberg, R.H., Hu, C., Zheng, L., 2011c. Trajectory forecast as a rapid response to the Deepwater Horizon oil spill. In: Monitoring and Modeling the Deepwater Horizon Oil Spill: A Record-Breaking Enterprise. In: Geophysical Monograph Series, vol. 195, pp. 153–165. http://dx.doi.org/10.1029/2011GM001121.

Ma, Z., Riishøjgaard, L.P., Masutani, M., Woollen, J.S., Emmitt, G.D., 2015. Impact of different satellite wind lidar telescope configurations on NCEP GFS forecast skill in observing system simulation experiments. J. Atmos. Ocean. Technol. 32 (3), 478–495.

Mayer, D.A., Weisberg, R.H., Zheng, L., Liu, Y., 2017. Winds on the West Florida Shelf: Regional comparisons between observations and model estimates. J. Geophys. Res. Oceans 122 (2), 834–846.

Mudele, O., Frery, A.C., Zanandrez, L.F., Eiras, A.E., Gamba, P., 2021. Dengue vector population forecasting using multisource earth observation products and recurrent neural networks. IEEE J. Sel. Top. Appl. Earth Obs. Remote Sens. 14, 4390–4404.

Nogueira, M., 2020. Inter-comparison of ERA-5, ERA-interim and GPCP rainfall over the last 40 years: Process-based analysis of systematic and random differences. J. Hydrol. 583, 124632.

Noman, F., Alkawsi, G., Alkahtani, A.A., Al-Shetwi, A.Q., Tiong, S.K., Alalwan, N., Ekanayake, J., Alzahrani, A.I., 2021. Multistep short-term wind speed prediction using nonlinear auto-regressive neural network with exogenous variable selection. Alex. Eng. J. 60 (1), 1221–1229.

Nordam, T., Beegle-Krause, C., Skancke, J., Nepstad, R., Reed, M., 2019. Improving oil spill trajectory modelling in the Arctic. Mar. Pollut. Bull. 140, 65–74.

Qi, P., Du, M., 2018. Multi-factor evaluation indicator method for the risk assessment of atmospheric and oceanic hazard group due to the attack of tropical cyclones. Int. J. Appl. Earth Obs. Geoinf. 68, 1–7.

Qiao, F., Wang, G., Yin, L., Zeng, K., Zhang, Y., Zhang, M., Xiao, B., Jiang, S., Chen, H., Chen, G., 2019. Modelling oil trajectories and potentially contaminated areas from the Sanchi oil spill. Sci. Total Environ. 685, 856–866.

Raimondi, V., Palombi, L., Lognoli, D., Masini, A., Simeone, E., 2017. Experimental tests and radiometric calculations for the feasibility of fluorescence LIDAR-based discrimination of oil spills from UAV. Int. J. Appl. Earth Obs. Geoinf. 61, 46–54.

Roberts, C.D., Senan, R., Molteni, F., Boussetta, S., Mayer, M., Keeley, S.P., 2018. Climate model configurations of the ECMWF Integrated Forecasting System (ECMWF-IFS cycle 43r1) for HighResMIP. Geosci. Model Dev. 11 (9), 3681–3712.

Röhrs, J., Dagestad, K.-F., Asbjørnsen, H., Nordam, T., Skancke, J., Jones, C.E., Brekke, C., 2018. The effect of vertical mixing on the horizontal drift of oil spills. Ocean Sci. 14 (6), 1581–1601.

Shivam, K., Tzou, J.-C., Wu, S.-C., 2020. Multi-step short-term wind speed prediction using a residual dilated causal convolutional network with nonlinear attention. Energies 13 (7), 1772.

Tang, R., Ning, Y., Li, C., Feng, W., Chen, Y., Xie, X., 2022. Numerical forecast correction of temperature and wind using a single-station single-time spatial LightGBM method. Sensors 22 (1), 193.

Toz, A., Koseoglu, B., 2018. Trajectory prediction of oil spill with Pisces 2 around Bay of Izmir, Turkey. Mar. Pollut. Bull. 126, 215–227.

Trebing, K., Mehrkanoon, S., 2020. Wind speed prediction using multidimensional convolutional neural networks. In: 2020 IEEE Symposium Series on Computational Intelligence. SSCI, IEEE, pp. 713–720.

Uppala, S.M., Kållberg, P., Simmons, A.J., Andrae, U., Bechtold, V.D.C., Fiorino, M., Gibson, J., Haseler, J., Hernandez, A., Kelly, G., et al., 2005. The ERA-40 reanalysis. Q. J. R. Meteorol. Soc. J. Atmos. Sci. Appl. Meteorol. Phys. Oceanogr. 131 (612), 2961–3012.

Weisberg, R.H., Lianyuan, Z., Liu, Y., 2017. On the movement of Deepwater Horizon Oil to northern Gulf beaches. Ocean Model. 111, 81–97.

Xingjian, S., Chen, Z., Wang, H., Yeung, D.-Y., Wong, W.-K., Woo, W.-c., 2015. Convolutional LSTM network: A machine learning approach for precipitation nowcasting. In: Advances in Neural Information Processing Systems. pp. 802–810.

Zhang, G., Li, X., Perrie, W., Hwang, P.A., Zhang, B., Yang, X., 2017. A hurricane wind speed retrieval model for C-band RADARSAT-2 cross-polarization ScanSAR images. IEEE Trans. Geosci. Remote Sens. 55 (8), 4766–4774.

Zhu, Q., Chen, J., Zhu, L., Duan, X., Liu, Y., 2018. Wind speed prediction with spatio–temporal correlation: A deep learning approach. Energies 11 (4), 705.

Zhuo, W., Fang, S., Gao, X., Wang, L., Wu, D., Fu, S., Wu, Q., Huang, J., 2022. Crop yield prediction using MODIS LAI, TIGGE weather forecasts and WOFOST model: A case study for winter wheat in Hebei, China during 2009–2013. Int. J. Appl. Earth Obs. Geoinf. 106, 102668.

Zjavka, L., 2015. Wind speed forecast correction models using polynomial neural networks. Renew. Energy 83, 998–1006.

Zodiatis, G., Lardner, R., Alves, T.M., Krestenitis, Y., Perivoliotis, L., Sofianos, S., Spanoudaki, K., 2017. Oil spill forecasting (prediction). J. Mar. Res. 75 (6), 923–953.